Climate Dynamics (2026) 64:332
https://doi.org/10.1007/s00382-026-08295-w

ORIGINAL ARTICLE

Extreme precipitation plays a major role in the intraseasonal progressive evolution of pre-flood precipitation in South China

Taichen Feng[1,2] · Huayin Wu[3] · Shen Lai[4] · Bicheng Huang[3,2] · Wenjie Dong[2,5] · Jianping Huang[6,7]

Received: 5 March 2026 / Accepted: 25 June 2026 / Published online: 15 July 2026

Abstract
Extreme precipitation plays an increasingly important role in pre-flood-season (April-June) precipitation over South China, yet its intraseasonal evolution and interdecadal shifts remain unclear. Observations from 1961 to 2024 show that total precipitation undergoes clear intraseasonal reorganization from April weakening to May near-neutral and June strengthening. Interdecadal turning points occur progressively later (April ~ 1984, May ~ 1990, June ~ 1992), and extreme precipitation contributes substantially the associated changes. The proportion of extreme precipitation to total precipitation (PEPTP) decreases in April (31.2 to 28.2%), remains nearly unchanged in May (31.0 to 30.4%), and increases in June (31.1 to 33.9%). This reflects a stepwise transition in the moisture-cold-air background: cold air dominated (April), enhanced moisture with weak cold air forcing (May), and a developed monsoon convergence regime (June), modulated by the tropical Atlantic, the tropical North Pacific, and the North Atlantic-Indian Ocean coupling. These results highlight the dominant role of extreme precipitation in shaping both intraseasonal and interdecadal pre-flood-season precipitation variability.

Keywords South China pre-flood season · Extreme precipitation contribution · Intraseasonal reorganization · Interdecadal variability

1 Introduction

Global warming has significantly increased the frequency and intensity of extreme precipitation, which is projected to intensify further under continued warming (Myhre et al. 2019; Mukherjee et al. 2018). In the United States, both the frequency and intensity of extreme precipitation have risen markedly since the 1990s (Jong et al. 2024; Dommo et al. 2024; Kunkel et al. 2020). In Europe, extreme precipitation already accounts for nearly 50% of the annual precipitation, and more than 62% of the region has experienced increases exceeding 10% in the contribution of extremes (Goffin et al. 2024). Under high-emission scenarios, this contribution is expected to become even more pronounced, especially in humid East Asia, where mean precipitation is projected to increase by approximately 12% (Juzbašić et al. 2024). In southwestern China, the proportion of extreme precipitation to total precipitation (PEPTP) increased from 32.6% during the 1976–1980 baseline period to 35.5% during 2013–2017 (Zheng et al. 2022). Therefore, understanding how extreme precipitation changes under global warming and how it contributes to total precipitation is of particular importance.

✉ Bicheng Huang
huangbch@yzu.edu.cn

1 College of Atmospheric Sciences, Lanzhou University, Lanzhou, China

2 Southern Marine Science and Engineering Guangdong Laboratory (Zhuhai), Zhuhai, China

3 College of Physical Science and Technology, Yangzhou University, Yangzhou, China

4 Climate Center of Guangxi Zhuang Autonomous Region, Nanning, Guangxi, China

5 School of Atmospheric Sciences, and Key Laboratory of Tropical Atmosphere-Ocean System, Ministry of Education, Sun Yat-Sen University, Zhuhai, China

6 Collaborative Innovation Center for Western Ecological Safety, Lanzhou University, Lanzhou, China

7 Key Laboratory for Semi-Arid Climate Change of the Ministry of Education, College of Atmospheric Sciences, Lanzhou University, Lanzhou, China

Extreme precipitation in China exhibits distinct spatial patterns and pronounced regional disparities over recent decades (Lu et al. 2024; Sun and Zhang 2017). Since 1961, both annual total precipitation and precipitation intensity have increased, displaying a gradient from the arid northwest toward the humid southeast (Zhou and Yuan 2024; Jiang et al. 2022). Gao and Xie (2014) reported that over the past 50 years, the frequency of extreme precipitation has increased across parts of the middle and lower reaches of the Yangtze River, whereas it has declined in northern, northeastern, and southwestern China. Specifically, extreme precipitation in southern China remained relatively rare between the late 1970s and early 1990s but has become increasingly frequent thereafter (Lu et al. 2010). Consequently, southern China has become highly vulnerable to extreme precipitation events (Zhang and Zhou 2020; Tang and Hu 2022; Huang et al. 2023). Among these regions, South China—owing to its unique geographic setting, climatic background, and rapid urbanization (Wu et al. 2019, 2021; Yin et al. 2020; Huang et al. 2022)—has emerged as a representative hotspot of extreme precipitation variability (Zhang and Zhou 2020).

Approximately 40%–50% of the annual total precipitation and 50%–60% of the annual extreme precipitation occur during from April–June, defined as the pre-flood season (Gao et al. 2013; Gu et al. 2018; Guo et al. 2024; Wang et al. 2024a). In recent years, several record-breaking extreme pre-flood precipitation events have been observed, including those occurring in May–June 2022 (Cheng et al. 2023; Liu et al. 2023; Wang et al. 2024b; Xie et al. 2023) and in April 2024. Notably, the characteristics of these events vary substantially across the three months. In April, total precipitation exhibits a significant decreasing trend (Lu et al. 2021; Yang et al. 2022; Zhang et al. 2013), with a decline of approximately 17 mm per decade during 1979–2015 (Zhang and Zhou 2020). Although extreme precipitation is relatively infrequent in April, its occurrence often marks the onset of the flood season (Gao et al. 2016). In May, precipitation variability becomes more complex. Two major regime shifts occurred in the early 1990s and early 2000s (Chu et al. 2020). During this transitional period, extreme precipitation became more pronounced, characterized by stronger intensity, higher frequency (Guo et al. 2024; Wu et al. 2020a; Yang et al. 2024), as well as longer duration (Zeng and Wang 2022). In June, both the frequency and intensity of extreme precipitation increase substantially (Li et al. 2024; Yuan et al. 2019), largely driven by the enhancement of warm-sector precipitation (Wu et al. 2020b). Extreme precipitation peaks in both intensity and frequency during this month (Wu et al. 2020a, b), and events tend to last longer (Sun et al. 2018). Precipitation often concentrates within short time periods and is accompanied by record-breaking short-duration extremes (Pu et al. 2022). Moreover, trends in extreme and total precipitation are highly consistent (Chu et al. 2017), and extreme precipitation contributes substantially to total monthly precipitation (Chu et al. 2017; Li et al. 2014). These findings reveal a clear intraseasonal progression of extreme precipitation during the pre-flood season, with these characteristics becoming increasingly prominent.

However, the manner in which extreme precipitation differs among the pre-flood season (April–June) in South China—and the mechanisms by which these differences translate into the observed weakening–stable–enhancing intraseasonal evolution of precipitation—remain insufficiently understood. In particular, the extent to which extreme precipitation controls total precipitation through month-dependent interdecadal shifts, along with the associated circulation and SST-forcing mechanisms, has not been fully quantified. This study investigates pre-flood season precipitation over South China during 1961–2024 to assess whether extremes play a major role in total precipitation variability. By systematically comparing April, May, and June, we characterize the intraseasonal progression and interdecadal transitions of extreme precipitation, and quantify its contribution to monthly totals, and elucidate the underlying mechanisms.

2 Data and methods

2.1 Datasets

Daily precipitation data from more than 2,400 national meteorological stations across mainland China for 1961–2024 were obtained from the National Meteorological Information Center (NMIC, http://data.cma.cn). The gridded versi on (Wu et al. 2017; Hersbach et al. 2023) was also used to test the robustness of the results. CN05.1 employs anomaly-based interpolation to produce a 0.25° × 0.25° dataset based on quality-controlled station observations (Ge et al. 2023; Yang et al. 2023). Monthly atmospheric circulation fields—including geopotential height, winds, vertical velocity, and specific humidity—were obtained from the ERA5 reanalysis. Monthly sea surface temperature (SST) fields were taken from NOAA ERSSTv5 (Huang et al. 2017). To ensure spatial compatibility, ERA5 fields were bilinearly interpolated to a common 2° × 2° grid before analysis. Large-scale climate indices used include the Indian Ocean Basin Mode (SST anomalies averaged over 20°S–20°N, 40°–100°E) (Feng and Chen 2022), and the tropical Atlantic warming index (TA, SST anomalies averaged over 20°S–20°N, 40°W–0°). This study focuses on the pre-flood season (April–June) precipitation in South China, represented by Guangxi and Guangdong provinces (Fig. S1). All anomalies are defined as deviations from the monthly climatological mean over 1961–2024.

2.2 The definition of extreme precipitation

To determine extreme precipitation thresholds, we adopted the percentile method proposed by Zhou and Ren (2011) with modifications. Given the non-negative, right-skewed, and heavy-tailed nature of daily precipitation sequences, which often include numerous extreme values, we employed the Gamma distribution to fit the data (Gu et al. 2021). The Gamma distribution effectively captures these characteristics and provides explicit parameters, facilitating the definition of extreme precipitation thresholds in conjunction with percentile values. In contrast, the Poisson distribution, as a single-parameter discrete probability distribution, may inadequately represent the complexity of the data. Similarly, the Ksdensity function requires larger datasets for stable estimates and may lack robustness when handling extreme values (Farmer and Jacobs 2022). The probability density function of the Gamma distribution is defined as follows:

$$f\left(x;k,\theta\right)=\frac{x^{k-1}e^{-x/\theta}}{\theta^{k}\Gamma\left(k\right)} \tag{1}$$

where k is the shape parameter, θ is the scale parameter, and $\Gamma(k)$ denotes the Gamma function.

In this study, precipitation equal to or greater than the 95th percentile threshold is classified as extreme precipitation. Following Li et al (2023), we defined daily precipitation exceeding 1 mm at each station as effective precipitation. Based on daily effective precipitation during the 1961–1990 reference period, a 95th percentile threshold is obtained by fitting the Gamma function to each day of the month. For each month, the monthly representative extreme precipitation threshold was defined as the median of the daily 95th percentile thresholds within that month. The method used to select thresholds (the percentile-based method median or mean of 95th percentile threshold) have a negligible impact on the main conclusions of this study (Fig. S2).

2.3 Proportion of extreme precipitation to total precipitation (PEPTP)

Based on daily precipitation at stations, we accumulate the precipitation above the threshold (the 95th percentile) for a given month and divide by the total precipitation for that month. The PEPTP were calculated as:

$$PEPTP=\left(\frac{R95p}{TP}\right)\times 100\% \tag{2}$$

where R95p represents the precipitation amount above 95th percentile and TP represents the total precipitation at stations for a given month. First, station PEPTP data are interpolated to South China and use only the data within the South China region to make the regional average to obtain the contribution rate of extreme precipitation in South China for this month.

2.4 Diagnostic of rossby wave energy dispersion

To diagnose the origin and downstream dispersion of Rossby wave trains, the phase-independent stationary wave activity flux (WAF) was formulated according to Takaya and Nakamura (2001):

$$W=\frac{1}{2\left|\overline{U}\right|}\left[\begin{array}{c}\overline{u}\left(\psi'^{2}_{x}-\psi'\psi'_{xx}\right)+\overline{v}\left(\psi'_{x}\psi'_{y}-\psi'\psi'_{xy}\right)\\ \overline{u}\left(\psi'_{x}\psi'_{y}-\psi'\psi'_{xy}\right)+\overline{v}\left(\psi'^{2}_{y}-\psi'\psi'_{yy}\right)\end{array}\right] \tag{3}$$

where U (u, v) is horizontal velocity, u and v are zonal and meridional wind velocity for June climatology mean over 1961–2024, and ψ' is perturbation stream function. Streamfunction values were computed using the 200hPa wind field, following standard geostrophic approximation:

$$\psi=\frac{\phi}{f} \tag{4}$$

where Φ is the geopotential, and f is the Coriolis parameter. Streamfunction is computed from ERA5 wind fields using geostrophic approximation and used here instead of geopotential height to ensure conservation properties required for diagnosing stationary Rossby wave propagation. Subscripts denote partial derivatives in zonal (x) and meridional (y) directions. The statistical significance of correlation and grid-point linear regression is assessed using a two-tailed Student's t test.

2.5 Causal information flow

Causal information flow quantifies the directed influence exerted by one time series upon another. In this framework, if event A possesses no causal impact on event B, they are treated as independent, resulting in a vanishing information flow. Conversely, a statistically significant non-zero flow signifies a robust causal link. Grounded in stochastic dynamical system theory, the rate of information flow from X_2 to X_1 (Liang and Kleeman 2005):

$$T_{2\to1}=-E\left(\frac{1}{\rho_1}\frac{\partial\left(F_1\rho_1\right)}{\partial x_1}\right)+\frac{1}{2}E\left(\frac{1}{\rho_1}\frac{\partial^2\left(b_{11}^2+b_{12}^2\right)\rho_1}{\partial x_1^2}\right) \tag{5}$$

where E denotes the mathematical expectation, and $\rho_1 = \rho_1$ (x_1) is the marginal probability density function of X_1. Under a linear assumption, Eq. (5) is further simplified into a maximum likelihood estimator (Liang, 2014):

$$T_{2\to 1} = \frac{C_{11}C_{12}C_{2,d1} - C_{12}^2 C_{1,d1}}{C_{11}^2 C_{22} - C_{11}C_{12}^2} \tag{6}$$

where C_{ij} are covariance terms and $C_{i,dj}$ are covariances with time derivatives. A non-zero information flow $T_{2\to 1}$ indicates a causal influence from variable X_2 to variable X_1. Moreover, the sign of $T_{2\to 1}$ reflects the direction of predictability: if $T_{2\to 1}>0$, then X_2 increases the uncertainty of X_1 and reducing its predictability; whereas if $T_{2\to 1}<0$, then X_2 enhances the predictability of $X_1$by reducing its entropy. The unit for $T_{2\to 1}$ is nats per unit time, and a z-test is applied to evaluate statistical significance.

3 Results

3.1 Intraseasonal progression of precipitation during the pre-flood season

Observational records from 1961–2024 show that although the mean pre-flood-season precipitation over South China remains broadly stable (Fig. S4a), its intraseasonal distribution has undergone systematic reorganization, exhibiting a pronounced month-to-month progression. Total precipitation decreases in April, shows no significant change in May, and increases in June (Fig. S3). The daily precipitation evolution further highlights this feature: precipitation weakens in April, remains near-normal in May, and intensifies markedly in June (Fig. S4b). Comparing the last decade with the first decade of the study period, April daily precipitation declines by more than 40%, whereas June daily precipitation remained above 1.5 times the baseline (Fig. S4c). We hypothesize that changes in extreme precipitation are a key driver of this intraseasonal reshaping. To test this, an 11-year moving *t*-test was applied to both total precipitation and extreme precipitation (Fig. S5). Results indicate significant interdecadal shifts, with progressively later turning points from April to June: April total and extreme precipitation both exhibit a robust regime shift around 1984 (exceeding the 95% confidence level); June total and extreme precipitation show a significant shift around 1992 (exceeding the 95% confidence level); while May displays weaker but consistent shift signals around 1990 in both total and extreme precipitation (exceeding the 90% confidence level). To assess the robustness of the identified interdecadal turning points, we repeated the moving *t*-test using 9-year and 13-year sliding windows and further applied the Pettitt test. The results show that the turning points in April and June are relatively stable across different methods and window lengths, whereas the May signal is weaker and more sensitive to the selected method. These tests suggest that the interdecadal transitions in April and June are robust, while the May transition should be interpreted with caution. Therefore, May is regarded as a weaker transitional stage in the subsequent analysis. Moreover, quantitative decomposition demonstrates a substantial contribution from extremes. The precipitation difference before and after the shift was 15.0 mm month^{-1} in April, of which extremes contributed 6.6 mm month^{-1}; 15.0 mm month^{-1} in May, with 5.1 mm month^{-1} from extremes; and 18.4 mm month^{-1} in June, with extremes contributing 11.0 mm month^{-1}. The results show that extreme precipitation accounts for approximately 59.8% of the total precipitation increase in June, approximately 34% of the total precipitation decrease in May, and approximately 44% of the total precipitation decrease in April (Fig. S5). These substantial fractions indicate that extreme precipitation accounts for a considerable proportion of the interdecadal changes. Extreme precipitation contributes substantially to the intraseasonal and interdecadal evolution of pre-flood-season precipitation in South China, with its contribution being most pronounced in June. In April and May, extreme precipitation remains important, but non-extreme precipitation also plays a non-negligible role.

3.2 Proportion of extreme precipitation to total precipitation

We further examined the intraseasonal differences in the PEPTP between the pre-transition and post-transition periods. In April, the PEPTP decreases from 31.2% (1961–1984) to 28.2% (1985–2024), indicating a weakening dominance of extreme precipitation. After the turning point, the frequency of light-rain events increased significantly, and the occurrence of heavier precipitation events decreased (Fig. 1b). The boxplots revealed that the post-transition median fell below the pre-transition 25th percentile, and the post-transition 75th percentile was even lower than the pre-transition median. Although precipitation intensity strengthened after the shift, the intensification of individual events was insufficient to compensate for the reduced event frequency (red points in Fig. 1b), resulting in a pronounced decrease in total April precipitation.

In June, the PEPTP increases from 31.1% (1961–1992) to 33.9% (1993–2024), suggesting a strengthening dominance of extreme precipitation. June exhibits the largest contrast across the transition (Fig. 1f). In the boxplots, the post-transition median surpassed the pre-transition 75th percentile, and the post-transition 25th percentile approached

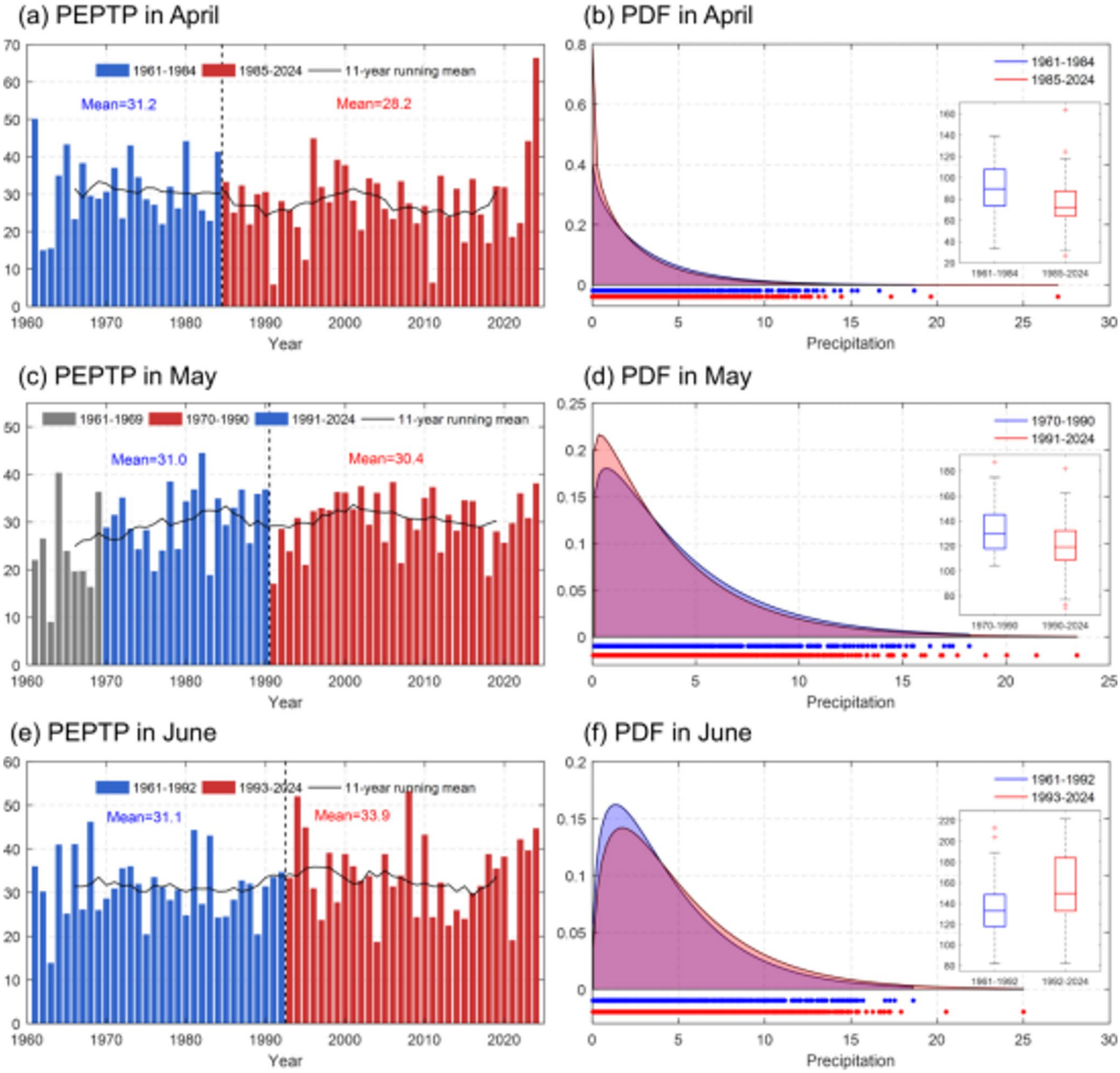

Fig. 1 The proportion of extreme precipitation to total precipitation (PEPTP, unit: %) in (**a**) April, (**c**) May, (**e**) June. The dashed lines represent the turning point of total precipitation (1984 in April, 1990 in May, and 1992 in June based on a sliding *t*-test). The black lines represent 11-year running mean of PEPTP. Shaded areas indicate statistically significant Gamma distribution fits to daily precipitation over South China before and after the turning point: (**b**) April, (**d**) May, (**f**) June. Observed daily precipitation values are marked with blue and red dots, respectively (unit: mm d^{-1}). Boxplot for month total precipitation from 1961 to 2024 (unit: mm $month^{-1}$). Blue (red) boxplots represent precipitation before (after) the turning point

the pre-transition median, reflecting a substantial intensification of extreme precipitation. Compared with April, both the frequency and intensity of extreme precipitation increased sharply, accompanied by a decrease in light-rain events. These changes directly led to a marked increase in total precipitation.

In contrast to April and June, May shows the smallest transition-related changes. The PEPTP decreases slightly from 31.0% (1970–1990) to 30.4% (1991–2024), suggesting that the dominance of extreme precipitation remains largely unchanged. The first ten years of May showed an increasing trend, but its duration was too short to be robust; consequently, these data were excluded from the statistical evaluation to ensure analytical reliability. Notably, although precipitation frequency decreased slightly after the turning point, the intensity of extreme precipitation increased substantially (red points in Fig. 1d). This intensification compensated for the reduction associated with fewer events, leading to minimal net change in total precipitation. Accordingly, May does not exhibit a clear abrupt shift, consistent with the weak significance in the moving *t*-test results (Fig. S4c and S4d). For May, the 11-year moving t-test suggests a possible turning point around 1990, but this signal is weaker and less robust than those in April and June. Although including the earliest 10 years produces an apparent weak increasing tendency over the full record, this feature is largely affected by the initial low-value period and does not indicate a robust abrupt change around 1990. Including this short initial segment may therefore bias the interdecadal comparison centered on the 1990 transition. When the comparison is confined to the periods immediately before and after 1990, PEPTP shows only a weak interdecadal decrease. Moreover, the tropical North Pacific SST signal exhibits a clear change in its relationship with PEPTP before and after 1990, supporting the use of 1990 as a reference year for the May analysis (Sect. 3.3). We therefore retain the original May comparison but now interpret the May turning point more cautiously.

3.3 Intraseasonal progression differences of PEPTP during pre-flood season

The intraseasonal evolution of pre-flood season precipitation from April to June exhibits a distinct "weakening–stabilizing–strengthening" pattern, driven by systematic changes in the configuration of moisture supply and cold-air activity, with moisture availability playing a critical role in modulating the intensity of extreme precipitation. The characteristics of the lower-tropospheric circulation before and after the interdecadal transition are shown in Fig. 2. In April, anomalous northwesterly and southwesterly winds prevail over South China and the northern South China Sea, indicating persistent cold-air intrusion from higher latitudes. The northwest Pacific anticyclone remains weak and displaced eastward, limiting the northward transport of warm, moist air from the Bay of Bengal (Fig. 3b). Although low-level southerlies strengthen after the transition (1985–2024), the vertically integrated moisture flux shows weak convergence over South China. This indicates that the strengthened low-level winds do not translate into an effective increase in moisture supply, as moisture primarily originates from Indochina and the southerly moisture transport from the South China Sea remains limited. As a result, April precipitation is characterized by a "weak moisture–strong cold-air" configuration. This environment favors frequent cold-air outbreaks, increasing light-rain occurrence, while insufficient moisture depth suppresses the development and frequency of extreme events; even when convection occurs, its intensity cannot be sustained (Fig. 1b).

In May (1991–2024), the low-level circulation undergoes a marked reorganization. Although a well-defined moisture corridor extends from the tropical Indian Ocean and moisture convergence over South China is pronounced (Fig. 3d), an anomalous anticyclone to the north and a cyclone to the south weaken the southward intrusion of cold air (Fig. 2d). This "strong moisture–weak cold-air" configuration helps maintain the intensity of extreme precipitation, whereas the frequency of extreme events decreases. Reduced baroclinic forcing limits the number of triggering disturbances, leading to fewer precipitation events overall, but the enhanced moisture availability allows those events that do develop to reach higher precipitation efficiency and maintain strong intensity (Fig. 1d).

In June (1993–2024), the monsoon circulation is fully established. The northwestern Pacific anticyclone sustains strong moisture transport (Figs. 2f, 3f), and a strengthened convergence center over South China and substantially enhanced moisture fluxes further promote ascent. Consequently, June precipitation is characterized by a "strong moisture–strong cold-air" configuration. The coupling of abundant monsoonal water vapor with renewed dynamical lifting increases both convective instability and large-scale ascent, simultaneously increasing the frequency of extreme events and amplifying their intensity, while light-rain events are suppressed by the dominance of deep convection (Fig. 1f).

The interdecadal shifts in the dominance of extreme precipitation exhibit pronounced month-to-month differences. These differences arise from the evolving pathways of upper-tropospheric wave-energy propagation and their synergy with lower-tropospheric moisture–cold-air configurations, which collectively drive progressively delayed transitions from April to June. The regression patterns of the 200 hPa quasi-geostrophic streamfunction and horizontal wave activity flux onto the PEPTP index are shown in Fig. 4. In April (1961–1984), two prominent wave-activity flux pathways provide dynamical support for southward cold-air outbreaks: one extends from Eastern Europe to Mongolia along the polar-front jet, and the other extends from Eastern Europe to India along the subtropical jet. After the transition (1985–2024), although a pronounced "two troughs–one ridge" pattern prevails over the Eurasian mid- to high latitudes, the wave-activity flux is significantly weaker than in the earlier period, implying reduced downstream energy propagation and weakened cold-air forcing, thereby contributing to the decline in PEPTP.

In May, the early period features a strong wave-activity flux band extending from Mongolia to southern China, accompanied by significant negative geopotential height

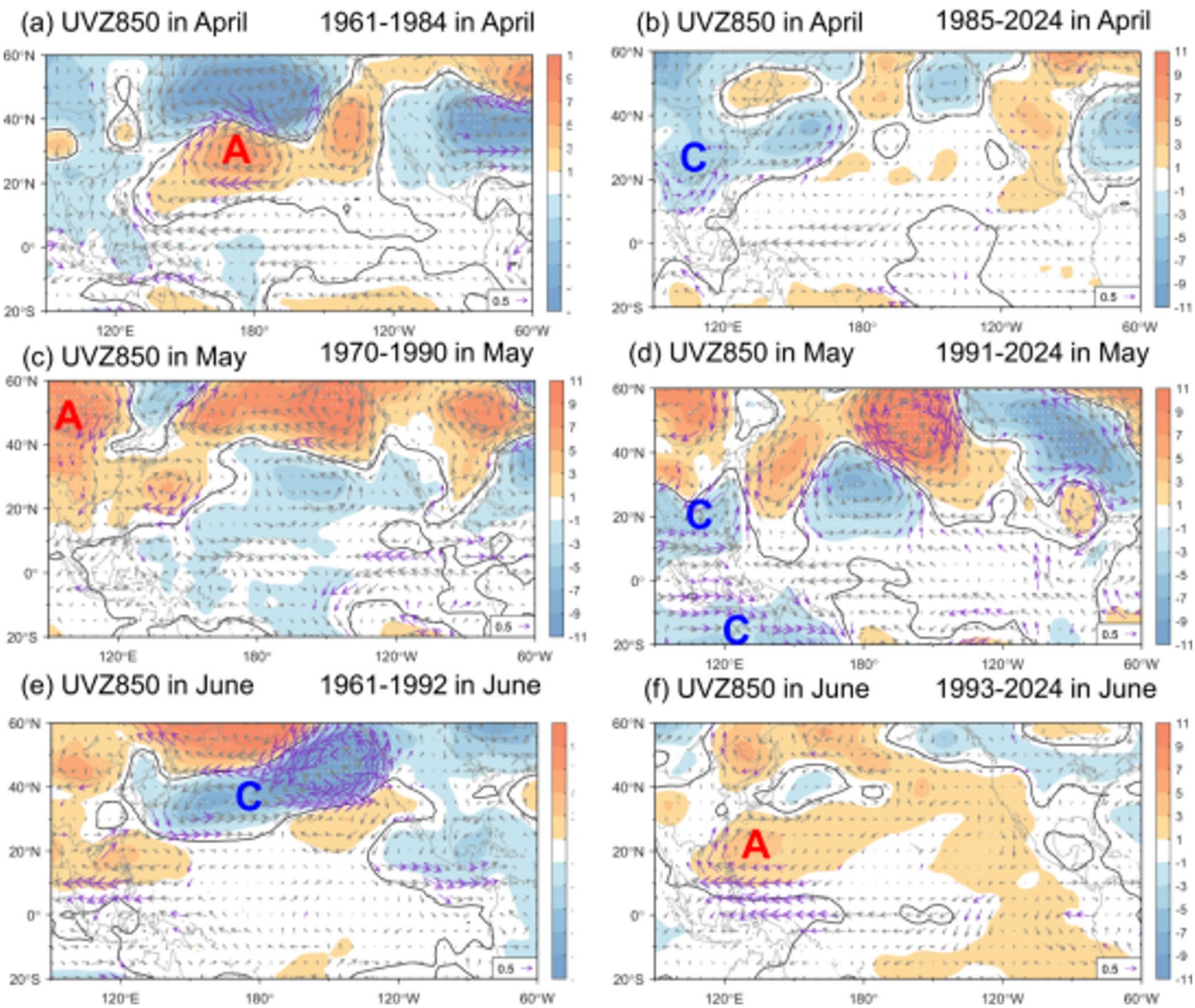

Fig. 2 Regression patterns of (**a**, **b**) April, (**c**, **d**) May, and (**e**, **f**) June mean anomalies of 850 hPa geopotential height (shading, unit: m) and wind fields (vector, unit: m s^{-1}) against the PEPTP index. Panels (**a**), (**c**), and (**e**) show the regression results for 1961–1984, 1970–1990, and 1961–1992, respectively, while panels (**b**), (**d**) and (**f**) correspond to 1985–2024, 1991–2024 and 1993–2024, respectively. Stippling indicates areas statistically significant at the 95% confidence level. The black outline marks China, and the red outline marks the South China domain analyzed in this study. "A" ("C") represents the anomalous anticyclone (cyclone)

anomalies over southern China, which favors cold-air intrusion and enhances low-level ascent. In the late period, the dominant wave-activity flux shifts to a pathway from India to southern China, while southward cold-air penetration is suppressed, contributing to a reduction in PEPTP.

In June, the wave-activity flux in the early period mainly extends from Western Europe to northern China, suggesting a relatively limited downstream influence on South China. In contrast, during the later period, the wave-activity flux exhibits a longer and more zonally continuous pathway from the Mediterranean region to northern China and subsequently to eastern China. This strengthened and more coherent downstream propagation indicates a closer linkage between upstream wave energy and circulation anomalies over eastern and southeastern China. Therefore, the enhanced downstream wave influence may provide a large-scale dynamic background more conducive to the increase in June PEPTP over South China.

These atmospheric adjustments are further modulated by sea surface temperature (SST) anomalies, the forcing patterns of which evolve systematically with the seasons. The SST anomaly patterns during the pre-transition and post-transition are shown in Fig. 5. In April, the most prominent differences between the two periods are the warming over the Indian Ocean and the tropical Atlantic (Fig. 5a and b). In May, the largest contrast is associated with a zonal dipole

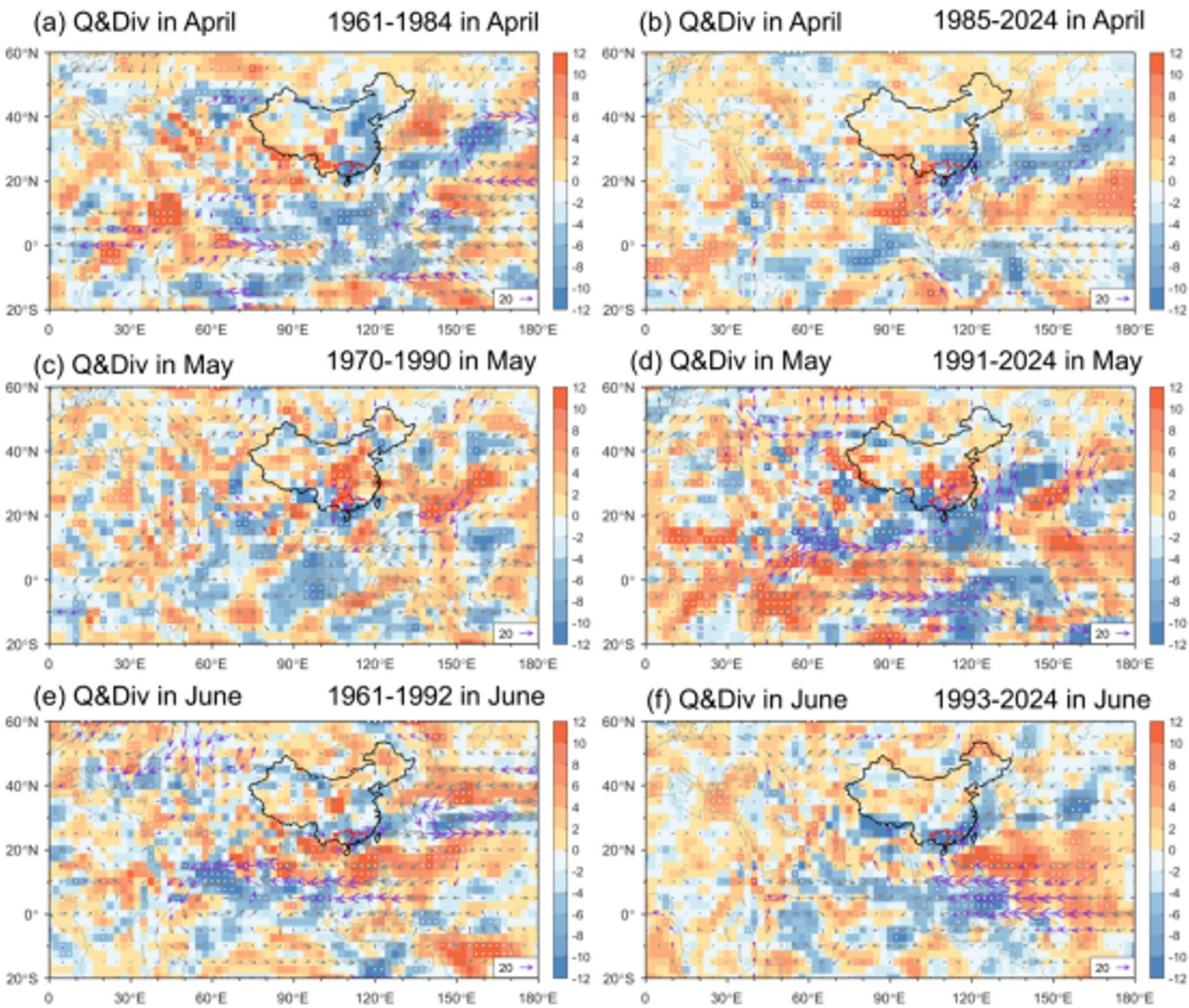

Fig. 3 Regression patterns of (**a**, **b**) April, (**c**, **d**) May, and (**e**, **f**) June mean vertically integrated water vapor flux from surface to 300hPa (vector, kg m^{-1} s^{-1}) and its divergence (shading, 10^{-6} kg m^{-2} s^{-1}) against the PEPTP index. Negative values of divergence indicate moisture convergence, while positive values indicate moisture divergence. Panels (**a**), (**c**), and (**e**) show the regression results for 1961–1984, 1970–1990, and 1961–1992, respectively, while (**b**), (**d**) and (**f**) correspond to 1985–2024, 1991–2024 and 1993–2024, respectively. Stippling indicates areas statistically significant at the 95% confidence level. The black outline marks China, and the red outline marks the South China domain analyzed in this study

pattern over the tropical North Pacific (Fig. 5c and d). In June, the strongest interdecadal difference is linked to a zonal dipole over the North Atlantic (Fig. 5e and f).

The key SST regions are selected according to a combined set of statistical and physical criteria rather than solely based on the spatial extent of significant SST regression signals. Specifically, we considered whether the SST anomalies in a given region: (1) exhibit a clear interdecadal change before and after the identified turning point; (2) are significantly correlated with PEPTP over South China; (3) show a statistically significant directional linkage to PEPTP in the information-flow analysis. Therefore, the selected SST indices are regarded as representative key SST signals that are closely linked to PEPTP variability, rather than as the only possible oceanic forcing regions. Other SST anomalies with significant regression signals may also contribute to the broader background variability, but were not selected as key indices unless they satisfied the above criteria. Accordingly, we define the tropical North Pacific zonal dipole index (TNP) as the principal component (PC) of the third EOF mode of SST anomalies over the region 120°E–90°W, 0–40°N, and the North Atlantic zonal dipole index (NAZD) as the PC of the third EOF mode over 70°W–0°, 40–60°N. Using these indices, we performed an 11-year running

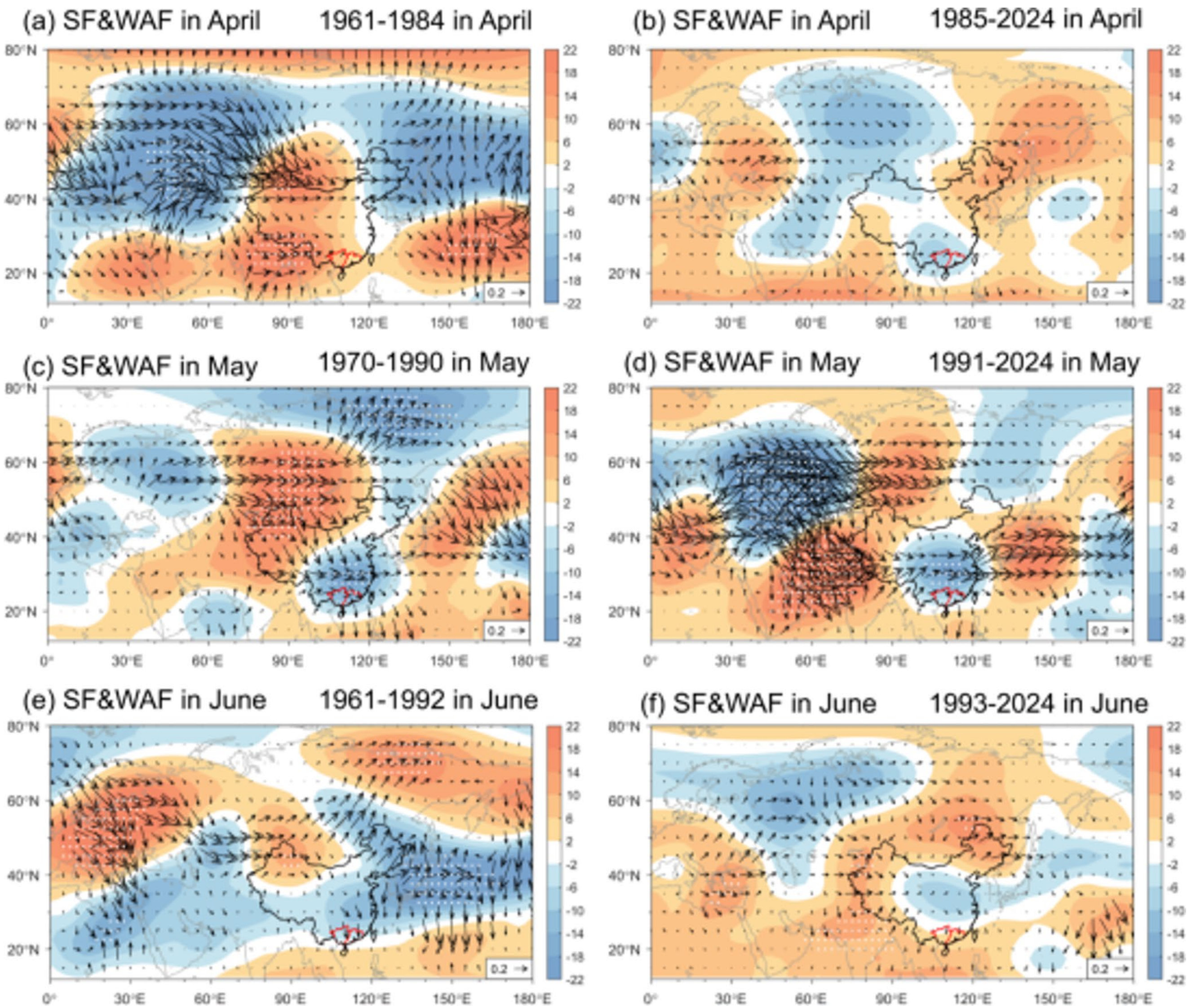

Fig. 4 Regressed patterns of 200hPa quasi-geostrophic streamfunction (shading; unit: 10^5 m^2 s^{-1}) and horizontal wave activity flux (vectors; unit: m^2 s^{-2}) onto the PEPTP index for (**a**, **b**) April, (c, d) May, and (**e**, **f**) June. Panels (**a**), (**c**), and (**e**) show the regression results for 1961–1984, 1970–1990, and 1961–1992, respectively, while (**b**), (**d**) and (**f**) correspond to 1985–2024, 1991–2024 and 1993–2024, respectively. Stippling indicates areas statistically significant at the 95% confidence level. The black outline marks China, and the red outline marks the South China domain analyzed in this study

causal analysis between each index and the PEPTP (Fig. 5g–i). The results indicate that, after the transition, tropical Atlantic SST anomalies may contribute to April PEPTP, the TNP becomes significantly linked to May PEPTP, and the NAZD is associated with June PEPTP during 1993–2024. Additionally, the tropical Indian Ocean warming exerts a significant influence.

To further examine the robustness of the SST–PEPTP relationship, we calculated the correlations between PEPTP and the corresponding key SST signal before and after the identified turning points for April, May, and June. As shown in Table 1, the correlations before the turning points are weak and statistically insignificant in all three months, with correlation coefficients of 0.08 in April, −0.09 in May, and 0.13 in June. In contrast, the correlations become stronger after the turning points, reaching 0.30 in April, 0.37 in May, and 0.40 in June. The post-transition correlations are statistically significant in May and June at the 95% confidence level, while the April correlation is marginally significant at approximately the 90% confidence level. These results indicate that the association between the key SST signals and PEPTP becomes more evident after the interdecadal transition, especially in May and June. Nevertheless, these correlation results, together with the information-flow analysis, should be interpreted as evidence of statistical association or directional influence rather than definitive proof

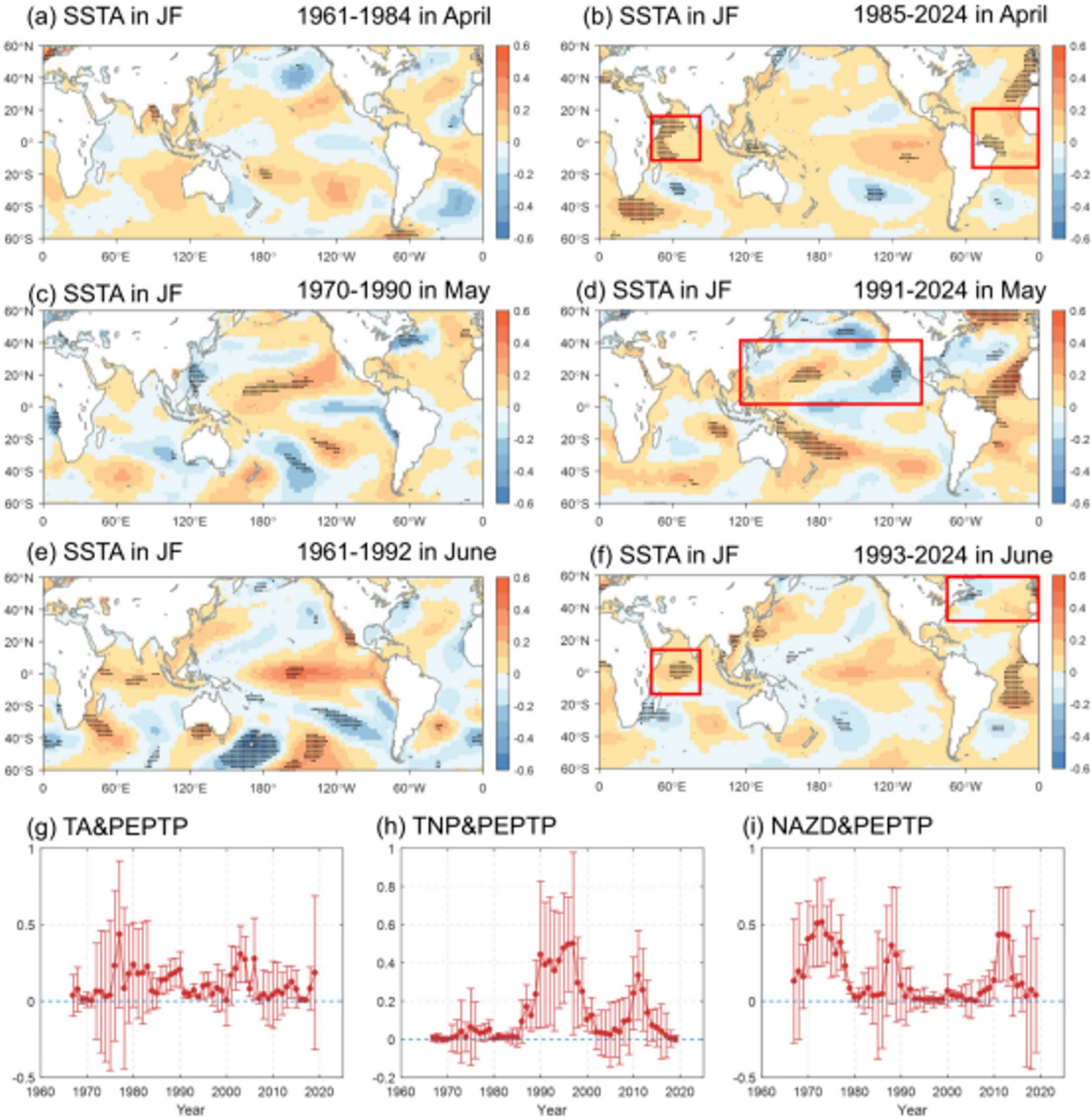

Fig. 5 Regression patterns of Sea Surface Temperature (SST) anomalies in January–February (unit: °C) onto the PEPTP index. Panels (**a**), (**e**), and (**b**) show the regression results for 1961–1984, 1970–1984, and 1961–1992, respectively, while (**b**), (**d**), and (**f**) correspond to 1985–2024, 1991–2024 and 1993–2024, respectively. Stippling indicates areas statistically significant at the 95% confidence level. (**g–i**) 11-year sliding-window information flow of (**g**) TA, (**f**) TNP, and (**g**) NAZD to the PEPTP (unit: nats year^{-1}). Error line not crossing the zero line (blue) indicate statistical significance at the 90% confidence level

Table 1 Correlations between PEPTP and the key SST signal before and after the turning point

Month	Before turning point	After turning point
April (TA)	0.08, $p = 0.73$	0.30, $p = 0.06$
May (TNP)	− 0.09, $p = 0.70$	0.37, $p = 0.03$
June (NAZD)	0.13, $p = 0.49$	0.40, $p = 0.02$

of dynamical causality. Therefore, the SST anomalies identified here are described as factors that may modulate, or are associated with, the changes in PEPTP through their linkage with large-scale circulation and moisture transport anomalies.

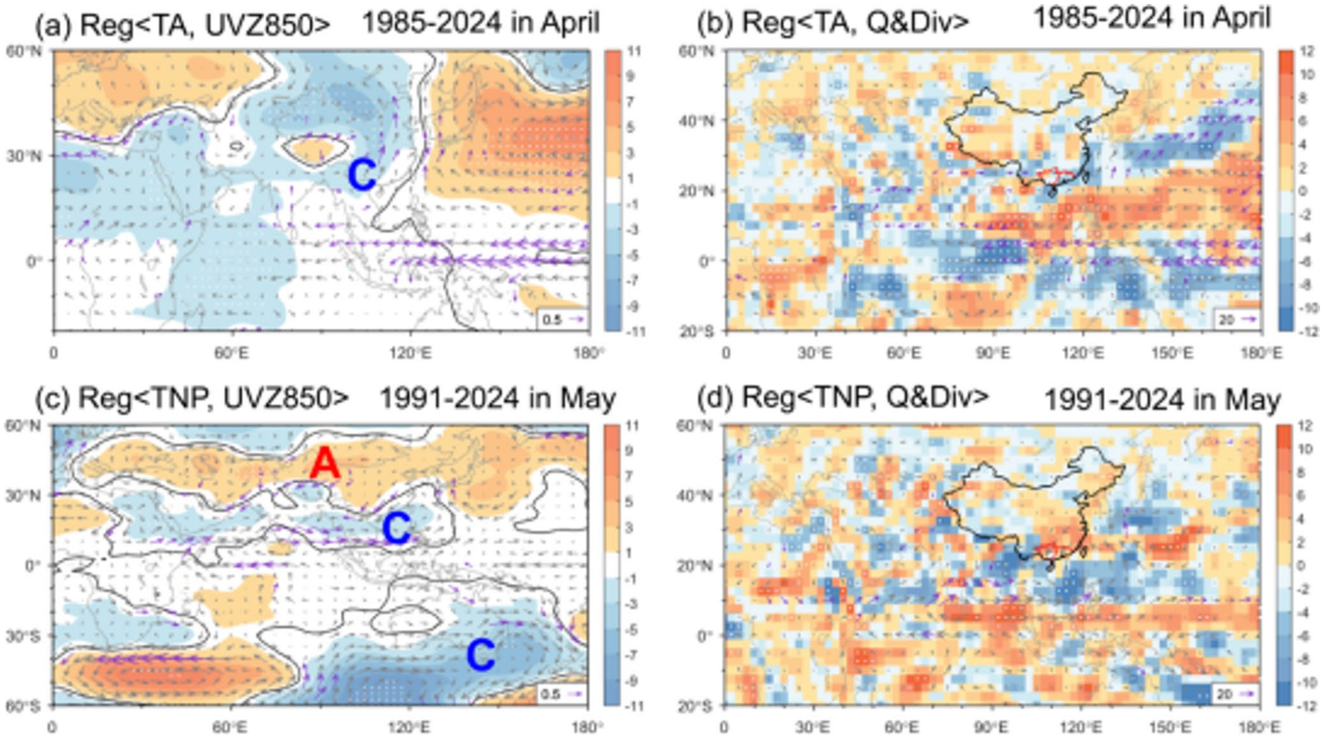

Fig. 6 Regression coefficients of (**a**) 850 hPa geopotential height (shading, unit: m) and wind fields (vector, unit: m s^{-1}) (**b**) mean vertically integrated water vapor flux from surface to 300hPa (vector, kg m^{-1} s^{-1}) and its divergence (shading, 10^{-6} kg m^{-2} s^{-1}) in April onto the standardized TA index during 1985–2024, Regression coefficients of (**c**) 850 hPa geopotential height (shading, unit: m) and wind fields (vector, unit: m s^{-1}) (**d**) mean vertically integrated water vapor flux from surface to 300hPa (vector, kg m^{-1} s^{-1}) and its divergence (shading, 10^{-6} kg m^{-2} s^{-1}) in May onto the standardized TNP index during 1985–2024. "A" ("C") represents the anomalous anticyclone (cyclone). Stippling indicates areas statistically significant at the 95% confidence level. The black outline marks China, and the red outline marks the South China domain analyzed in this study

These atmospheric adjustments are further modulated by these SST indices. In April, warming over the tropical Atlantic modulates the Walker circulation, inducing anomalous subsidence over the equatorial central Pacific and suppressing convection. Through a Gill-type response, an anomalous anticyclone develops to the north of the suppressed convective region, shifting the northwest Pacific anticyclone eastward (Fig. 6a) (Zhang et al. 2023). This configuration favors a southward extension of the East Asian trough, facilitating cold-air intrusions into South China. In May, the enhanced Pacific zonal SST gradient strengthens the low-level zonal winds (Fig. 6c). This circulation adjustment also promotes moisture transport from the Indian Ocean toward South China (Fig. 6d), but meanwhile suppresses the southward intrusion of mid- to high-latitude cold air. Although the enhanced moisture transport favors stronger precipitation intensity in May, the suppressed southward intrusion of mid- to high-latitude cold air weakens the dynamical lifting conditions required for extreme precipitation. Therefore, precipitation intensity may increase, while the PEPTP shows only a weak decrease or remains nearly stable. The June SST-related regression patterns are not reproduced in Fig. 6 because they have been systematically presented in Feng et al. (2025). In brief, the post-1993 increase in June PEPTP reflects a stronger multi-basin oceanic influence: the NAZD, in conjunction with tropical Indian Ocean warming, which together modulate the mid-latitude westerlies and the subtropical jet, substantially enhancing southwesterly moisture transport and convergence over South China (Feng et al. 2025).

The progressively later turning points from April to June likely reflect a transition in the dominant oceanic forcing, characterized by shifts in both latitude and coupling complexity. On the one hand, the key SST signals propagate from the tropics toward the mid- to high latitudes, and such extratropical responses typically involve extended adjustment timescales (e.g., via air–sea interaction and downstream wave-train development), contributing to a delayed emergence of circulation and precipitation regime shifts. On the other hand, the dominant drivers evolve from a single-basin signal in April–May to a multi-basin coupled influence in June, when the Indian Ocean and North Atlantic act synergistically. This inter-basin coordination requires a more integrated atmospheric adjustment, which can further delay the occurrence of the detectable interdecadal transition. Nevertheless, the robustness of the turning points is not uniform across months. Additional sensitivity tests show that the April and June transitions are relatively stable, whereas the May turning point is weaker and more sensitive to the detection method. Therefore, May is interpreted as a transitional month, and the 1990 turning point is retained only as a reference year for interdecadal comparison. The overall feature of a progressively delayed transition from April to June is mainly supported by the robust changes in April and June.

4 Conclusions and discussion

This study documents a robust intraseasonal reorganization of the pre-flood season precipitation (April–June) over South China during 1961–2024. The key findings reveal that changes in extreme precipitation are highly consistent with those in total precipitation and explain the substantial fraction of the interdecadal differences, indicating that extreme precipitation plays a leading role in shaping the interdecadal variability of pre-flood season precipitation. The dominance of extreme precipitation exhibits clear month-dependent interdecadal transitions: it weakens in April (31.2 to 28.2%), remains nearly unchanged in May (31.0 to 30.4%), and strengthens in June (31.1 to 33.9%). These differences arise from distinct combinations of event frequency and intensity changes across months. The corresponding circulation evolution shows a stepwise transition in the moisture–cold-air configuration: April is dominated by the weak moisture–strong cold-air regime, May features strong moisture but weakened cold-air intrusion, favoring high event intensity but reduced frequency, and June is characterized by a strong moisture–strong forcing environment associated with a mature monsoon circulation and enhanced convergence. The turning points occur progressively later from April to June, consistent with a seasonal shift from relatively direct tropical forcing toward stronger mid-latitude involvement and more complex multi-basin coupling.

The intraseasonal evolution of PEPTP is governed by the combined modulation of moisture supply and dynamical triggering: moisture primarily determines the intensity of extremes, whereas cold-air intrusion and ascent influence the occurrence and organization of events. These interdecadal shifts are further linked to seasonally evolving SST forcing, with forcing related to tropical Atlantic being more relevant in April, the tropical North Pacific zonal dipole in May, and the combined North Atlantic–Indian Ocean influence becoming more significant in June. These results suggest that monitoring key SST patterns may improve month-specific predictability of pre-flood season extremes over South China.

Several issues warrant further investigation. First, the causal analysis relies on statistical information flow and thus cannot fully replace dynamical attribution. Numerical model sensitivity experiments are required to isolate basin-specific roles and interactions. Second, the changes in synoptic/mesoscale systems should be quantified to better explain the April decrease and the strong June enhancement. In addition, given that the most extreme precipitation continues to intensify, the associated disaster risk is also increasing (Fig. 1); however, the response mechanisms of such extremes to global warming—and how these mechanisms differ from those governing general extreme precipitation—remain to be clarified. Finally, exploring how these operate under future warming will be essential for improving flood-risk outlooks over South China.

Supplementary Information The online version contains supplementary material available at https://doi.org/10.1007/s00382-026-08295-w.

Author contributions Taichen Feng: Writing—Original Draft. Huayin Wu: Writing—Original Draft, Visualization. Shen Lai: Methodology, Formal Analysis. Bicheng Huang: Writing—Review & Editing, Methodology. Wenjie Dong: Formal Analysis, Conceptualization. Jianping Huang: Formal Analysis, Conceptualization.

Funding This work was supported by the National Natural Science Foundation of China (42405028, 42405058, 42475059), and Research Fund of Arid Meteorology (IAM202413).

Data availability The CN05.1 precipitation data set can be available at https://ccrc.iap.ac.cn/resource/detail?id=228. The ERSSTv5 data set is available at Huang et al. (2017). The ERA5 reanalysis data are available at Hersbach et al. (2023).

Declarations

Conflict of interest The authors declare that they have no known competing financial interests or personal relationships that could have appeared to influence the work reported in this paper.

References

Cheng J, Zhao Y, Zhi R, Feng G (2023) Meridional circulation dominates the record-breaking “Dragon Boat Water” rainfall over South China in 2022. Front Earth Sci 10:1–12. https://doi.org/10.3389/feart.2022.1032313

Chu QC, Wang QG, Feng GL (2017) Determination of the major moisture sources of cumulative effect of torrential rain events during the preflood season over South China using a Lagrangian particle model. J Geophys Res Atmos 122:8369–8382. https://doi.org/10.1002/2016JD026426

Chu QC, Wang QG, Feng GL (2020) The roles of moisture transports in intraseasonal precipitation during the preflood season over South China. Int J Climatol 40:2239–2252. https://doi.org/10.1002/joc.6329

Dommo A, Aloysius N, Lupo A, Hunt S (2024) Spatial and temporal analysis and trends of extreme precipitation over the

Mississippi River Basin, USA during 1988–2017. J Hydrol Reg Stud 56:101954. https://doi.org/10.1016/j.ejrh.2024.101954

Farmer J, Jacobs DJ (2022) MATLAB tool for probability density assessment and nonparametric estimation. SoftwareX 18:101017. https://doi.org/10.1016/j.softx.2022.101017

Feng J, Chen W (2022) Respective and combined impacts of North Indian Ocean and Tropical North Atlantic SST anomalies on the subseasonal evolution of anomalous Western North Pacific anticyclones. J Clim 35:5623–5636. https://doi.org/10.1175/JCLI-D-21-0799.1

Feng T, Wu H, Lai S et al (2025) Interdecadal increase of the contribution of extreme precipitation in June in South China. Geophys Res Lett 52:e2025GL117366. https://doi.org/10.1029/2025GL117366

Gao H, Jiang W, Li WJ (2013) Transition of the annual cycle of precipitation from double-peak mode to single-peak mode in South China. Chin Sci Bull 58:3994–3999. https://doi.org/10.1007/s11434-013-5905-0

Gao J, Lin H, You L, Chen S (2016) Monitoring early-flood season intraseasonal oscillations and persistent heavy rainfall in South China. Clim Dyn 47:3845–3861. https://doi.org/10.1007/s00382-016-3045-3

Gao T, Xie L (2014) Study on progress of the trends and physical causes of extreme precipitation in China during the last 50 years. Adv Earth Sci 29:577–589. https://doi.org/10.11867/j.issn.1001-8166.2014.05.0577

Ge S, Jiang C, Wang J, Liu S (2023) Analyzing temperature and precipitation extremes in China using multiple gridded datasets: a comparative evaluation. Weather Clim Extrem 42:100614. https://doi.org/10.1016/j.wace.2023.100614

Goffin BD, Kansara P, Lakshmi V (2024) Intensification in the Wettest Days to 50 percent of annual precipitation (WD50) across Europe. Geophys Res Lett 51:e2023GL107403. https://doi.org/10.1029/2023GL107403

Gu W, Wang L, Hu ZZ et al (2018) Interannual variations of the first rainy season precipitation over South China. J Clim 31:623–640. https://doi.org/10.1175/JCLI-D-17-0284.1

Gu X, Ye L, Zhao T et al (2021) Probability distribution of daily precipitation in China. Shuili Xuebao/j Hydraul Eng 52:1248–1262. https://doi.org/10.13243/j.cnki.slxb.20201066

Guo ZH, Chen Y, Xiao TG, Zeng ZL (2024) Mesoscale and microphysical characteristics of a double rain belt event in South China on May 10–13, 2022. J Trop Meteorol 30:61–75. https://doi.org/10.3724/j.1006-8775.2024.007

Hersbach H, Bell B, Berrisford P, Biavati G, Horányi A, Muñoz Sabater J et al (2023) ERA5 monthly averaged data on pressure levels from 1940 to present. Copernicus Climate Change Service C3S) Climate Data Store (CDS). https://doi.org/10.24381/cds.6860a573

Huang H, Cui H, Singh VP (2023) Clustering daily extreme precipitation patterns in China. Water (Switzerland) 15:3651. https://doi.org/10.3390/w15203651

Huang X, Wang D, Ziegler AD et al (2022) Influence of urbanization on hourly extreme precipitation over China. Environ Res Lett 17:0044010. https://doi.org/10.1088/1748-9326/ac59a6

Jiang J, Zhou T, Zhang W (2022) Temporal and spatial variations of extreme precipitation in the main river basins of China in the past 60 years. Chin J Atmos Sci 46:707–724. https://doi.org/10.3878/j.issn.1006-9895.2111.21187

Jong BT, Murakami H, Delworth TL, Cooke WF (2024) Contributions of tropical cyclones and atmospheric rivers to extreme precipitation trends over the northeast US. Earth's Futur 12:e2023EF004370. https://doi.org/10.1029/2023EF004370

Juzbašić A, Park C, Cha DH et al (2024) The difference in the uncertainty sources between future projections of mean and extreme precipitation over East Asia. Environ Res Lett 19:074015. https://doi.org/10.1088/1748-9326/ad52ae

Kunkel KE, Karl TR, Squires MF et al (2020) Precipitation extremes: trends and relationships with average precipitation and precipitable water in the contiguous United States. J Appl Meteorol Climatol 59:125–142. https://doi.org/10.1175/JAMC-D-19-0185.1

Li LP, Zhang KM, Luo T, Fu X (2014) An analysis of the drought and flood hazard characteristics and risks during the pre-rainy season in South China. Nat Hazards 71:1195–1213. https://doi.org/10.1007/s11069-013-0692-0

Li X, Wang D, Zhou W (2024) Multiple-time-scale variations of the record-breaking pre-summer rainfall over South China in 2022. J Clim 37:1965–1980. https://doi.org/10.1175/JCLI-D-23-0586.1

Li Y, Liu M, Sun J, Zhao Y (2023) Analysis of extreme precipitation event characteristics and typical events based on the intensity–area–duration method in Liaoning Province. Theor Appl Climatol 152:201–211. https://doi.org/10.1007/s00704-023-04381-9

Liang XS (2014) Unraveling the cause-effect relation between time series. Phys Rev E—Stat Nonlinear, Soft Matter Phys 90:052150. https://doi.org/10.1103/PhysRevE.90.052150

Liang XS, Kleeman R (2005) Information transfer between dynamical system components. Phys Rev Lett 95:1–4. https://doi.org/10.1103/PhysRevLett.95.244101

Liu B, Zhu C, Xu K et al (2023) Record-breaking pre-flood rainfall over South China in 2022: role of historic warming over the Northeast Pacific and Maritime Continent. Clim Dyn 61:3147–3163. https://doi.org/10.1007/s00382-023-06734-6

Lu H, He H, Chen SR (2010) Spatiotemporal variation of extreme precipitation frequency in summer over South China in 1961–2008. Chinese J Ecol 29:1213–1220. https://doi.org/10.13292/j.1000-4890.2010.0177

Lu J, Wang K, Wu G, Mao Y (2024) Evaluation of multisource datasets in characterizing spatiotemporal characteristics of extreme precipitation from 2001 to 2019 in China. J Hydrometeorol 25:515–539. https://doi.org/10.1175/JHM-D-23-0162.1

Lu X, Li Q, Zhao W et al (2021) Spatiotemporal characteristics of rainfall in South China from 1967 to 2018. J Appl Meteorol Climatol 60:1333–1345. https://doi.org/10.1175/JAMC-D-20-0191.1

Mukherjee S, Aadhar S, Stone D, Mishra V (2018) Increase in extreme precipitation events under anthropogenic warming in India. Weather Clim Extrem 20:45–53. https://doi.org/10.1016/j.wace.2018.03.005

Myhre G, Alterskjær K, Stjern CW et al (2019) Frequency of extreme precipitation increases extensively with event rareness under global warming. Sci Rep 9:1–10. https://doi.org/10.1038/s41598-019-52277-4

Pu Y, Hu S, Luo Y et al (2022) Multiscale perspectives on an extreme warm-sector rainfall event over coastal South China. Remote Sens 14:3110. https://doi.org/10.3390/rs14133110

Sun J, Ming J, Zhang M, Yu S (2018) Circulation features associated with the record-breaking rainfall over south China in June 2017. J Clim 31:7209–7224. https://doi.org/10.1175/JCLI-D-17-0903.1

Sun J, Zhang FQ (2017) Daily extreme precipitation and trends over China. Sci China Earth Sci 60:2190–2203. https://doi.org/10.1007/s11430-016-9117-8

Takaya K, Nakamura H (2001) A formulation of a phase-independent wave-activity flux for stationary and migratory quasigeostrophic eddies on a zonally varying basic flow. J Atmos Sci 58:608–627. https://doi.org/10.1175/1520-0469(2001)058%3c0608:AFOAPI%3e2.0.CO;2

Tang B, Hu W (2022) Significant increase in population exposure to extreme precipitation in south China and Indochina in the future. Sustain 14:1–14. https://doi.org/10.3390/su14105784

Wang B, Wei W, Yin Z, Xu L (2024a) Using machine learning to analyze the changes in extreme precipitation in southern China. Atmos Res 302:107307. https://doi.org/10.1016/j.atmosres.2024.107307

Wang Z, Xu J, Zeng Z et al (2024b) Understanding the 2022 extreme dragon-boat rainfall in South China from the combined land and

oceanic forcing. Asia-Pac J Atmos Sci 60:1–14. https://doi.org/10.1007/s13143-024-00356-6
Wu J, Gao X, Giorgi F, Chen D (2017) Changes of effective temperature and cold/hot days in late decades over China based on a high resolution gridded observation dataset. Int J Climatol 37:788–800. https://doi.org/10.1002/joc.5038
Wu L, Hu F, Xie L (2020a) Characteristics of extreme precipitation in South China during April–July for early rice season. J Earth Syst Sci 129:189. https://doi.org/10.1007/s12040-020-01466-1
Wu M, Luo Y, Chen F, Wong WK (2019) Observed link of extreme hourly precipitation changes to urbanization over coastal South China. J Appl Meteorol Climatol 58:1799–1819. https://doi.org/10.1175/JAMC-D-18-0284.1
Wu N, Ding X, Wen Z et al (2020b) Contrasting frontal and warm-sector heavy rainfalls over South China during the early-summer rainy season. Atmos Res 235:104693. https://doi.org/10.1016/j.atmosres.2019.104693
Wu S, Chan TO, Zhang W et al (2021) Increasing compound heat and precipitation extremes elevated by urbanization in South China. Front Earth Sci 9:1–9. https://doi.org/10.3389/feart.2021.636777
Xie J, Hsu PC, Hu Y et al (2023) Disastrous persistent extreme rainfall events of the 2022 pre-flood season in South China: causes and subseasonal predictions. J Meteorol Res 37:469–485. https://doi.org/10.1007/s13351-023-3014-9
Yang L, Liang X, Yin J et al (2023) The extreme precipitation and added value of East Asia regional reanalysis system. Int J Climatol 43:6831–6850. https://doi.org/10.1002/joc.8238
Yang Y, Ren L, Wu M et al (2022) Abrupt emissions reductions during COVID-19 contributed to record summer rainfall in China. Nat Commun 13:1–7. https://doi.org/10.1038/s41467-022-28537-9
Yang Y, Jiang X, Wang X et al (2024) Isotopic characteristics of extreme “dragon-boat water” rainfall between mid-May and mid-June in 2022 in Fuzhou, southeastern China. J Hydrol 642:131870. https://doi.org/10.1016/j.jhydrol.2024.131870
Yin J, Zhang DL, Luo Y, Ma R (2020) On the extreme rainfall event of 7 May 2017 over the coastal city of Guangzhou. Part I: impacts of urbanization and orography. Mon Weather Rev 148:955–979. https://doi.org/10.1175/MWR-D-19-0212.1
Yuan C, Liu J, Luo JJ, Guan Z (2019) Influences of tropical Indian and Pacific Oceans on the interannual variations of precipitation in the early and late rainy seasons in South China. J Clim 32:3681–3694. https://doi.org/10.1175/JCLI-D-18-0588.1
Zeng Z, Wang D (2022) On the local rain-rate extreme associated with a mesovortex over South China: observational structures, characteristics, and evolution. Mon Weather Rev 150:1075–1096. https://doi.org/10.1175/MWR-D-21-0033.1
Zhang Q, Li J, Singh VP et al (2013) Influence of ENSO on precipitation in the East River basin, south China. J Geophys Res Atmos 118:2207–2219. https://doi.org/10.1002/jgrd.50279
Zhang S, Liu Y, Sheng C, Ma T (2023) Influence of boreal spring sea surface temperature anomalies over the tropical South Atlantic on the Meiyu onset. Clim Dyn 60:3613–3628. https://doi.org/10.1007/s00382-022-06483-y
Zhang W, Zhou T (2020) Increasing impacts from extreme precipitation on population over China with global warming. Sci Bull 65:243–252. https://doi.org/10.1016/j.scib.2019.12.002
Zheng G, Li Y, Chen Q et al (2022) The increasing predominance of extreme precipitation in Southwest China since the late 1970s. Atmos Ocean Sci Lett 15:100227. https://doi.org/10.1016/j.aosl.2022.100227
Zhou A, Yuan C (2024) Global warming intensifies once-in-a-decade extreme precipitation in summer in China. Atmos Ocean Sci Lett 18:100561. https://doi.org/10.1016/j.aosl.2024.100561
Zhou Y, Ren G (2011) Change in extreme temperature event frequency over mainland China, 1961–2008. Clim Res 50:125–139. https://doi.org/10.3354/cr01053